# Ultrahigh-Sensitivity Bragg Atom Gravimeter and its Application in Testing Lorentz Violation

Tao Zhang, Le-Le Chen, Yu-Biao Shu, Wen-Jie Xu, Yuan Cheng, Qin Luo, Zhong-Kun Hu,[*] and Min-Kang Zhou[†]

*MOE Key Laboratory of Fundamental Physical Quantities Measurement, Hubei Key Laboratory of Gravitation and Quantum Physics, PGMF, and School of Physics, Huazhong University of Science and Technology, Wuhan 430074, China*

We have demonstrated a precision atom-interferometry gravimeter based on matter-wave Bragg diffraction. By decreasing the atom temperature and increasing the atom number with Raman sideband cooling, it is shown that our Bragg atom gravimeter can achieve a short-term sensitivity of 2.2 μGal/Hz$^{1/2}$ (1 Gal = 1 cm/s$^2$), improved by nearly a factor of 2 compared to that of a state-of-the-art atom gravimeter. The resolution of our atom gravimeter has reached 0.08 μGal after an integration time of 2000 s, comparable to a cryogenic superconducting gravimeter. Based on extremely sensitive and stable gravity measurements, a test of local Lorentz invariance in the gravity sector was performed, where the accuracy of the upper bound on the space-space component was improved by a factor of 4.

## I. INTRODUCTION

The cold-atom-based interferometer is a promising quantum technology for inertial sensing, precision measurements, and testing of fundamental physics. The atom interferometer is widely used for high-precision measurements, such as the measurement of gravity [1–5] and its gradients [6], measuring rotation [7], determining the physical constants [8,9], probing magnetic fields [10], detecting gravitational waves [11,12], and testing the weak equivalence principle.

The equivalence principle is one of the cornerstones of Einstein's general theory of relativity, which mainly includes the universality of free fall, local position invariance, and local Lorentz invariance (LLI) [13,14]. The failure of general relativity to unify with the standard model suggests that one of its fundamental assumptions may be violated to some degree of accuracy [15]. Various experiments have been implemented to test the equivalence principle, such as tests of local position invariance by redshift measurements with atom interferometers and clocks [16,17], and tests of the universality of free fall with different matter [18–27]. Tests for LLI might exhibit the violations in the matter sector itself, or in the gravity sector as far as their coupling [28,29].

The violation of the LLI in the gravity sector manifests itself as a deviation in the direction of the force on the connecting line between the two bodies. Many experiments have been performed in the gravity sector to test the LLI, such as gravimetry [30–32], lunar laser ranging [33–35], and astrophysical observations [36,37]. When gravity is anisotropic, the local acceleration of a free-falling body on a rotating Earth should exhibit a modulation related to the Earth's rotation, which means that highly sensitive instruments such as cryogenic superconducting gravimeters, atom interferometers, etc. could hopefully test the LLI by detecting gravity violation.

With the development of quantum measurement techniques, the short-term sensitivity of atom-interferometry gravimeters has reached the state-of-the-art level [3–5,30]. The sensitivity of the atom-interferometry gravity gradiometer has reached the level that is limited by quantum projection noise [38]. The Raman-type atom-interferometry gravimeter has achieved 4.2 μGal/Hz$^{1/2}$, which is mainly limited by detection noise [4]. The Bragg atom interferometer has reached a sensitivity of 19 μGal/Hz$^{1/2}$ for gravity measurements, which is limited by phase noise and detection noise [39].

In this paper, we present absolute gravity measurements with a Bragg atom interferometer. First, we introduce the principle of gravity measurement with atom interferometers. We then introduce the principle of testing LLI with gravity data. Then we introduce our experimental system and show how to enhance the time-of-flight (TOF) signal of the experiment with Raman sideband cooling (RSC) and optical pumping. Then we state the experimental results of the gravity measurements and their noise limits. Finally,

we give experimental constraints on the LLI violation in the minimal standard model extension of the pure-gravity sector.

## II. PRINCIPLES

### A. Gravity measurement

The principle of the Mach-Zehnder atom gravimeter has been described in detail [40]. In this atom interferometer, the wave packet is split, reflected, and overlapped by a sequence of $\pi/2$-$\pi$-$\pi/2$ Bragg pulses to form interference, as shown in Fig. 1(a). Atoms with momentum state $|p_0\rangle$ interact with the Bragg $\pi/2$ pulse at point A and are divided into two beams. The momentum of one side is not changed, but the other side has increased its momentum by $n\hbar k_{\text{eff}}$, where $k_{\text{eff}} = k_1 - k_2$ is the effective wave vector of the Bragg pulse, and $n$ is the Bragg diffraction order. After time $T$, the atom interacts with the Bragg $\pi$ pulse. The atomic momentum of the upper path decreases by $n\hbar k_{\text{eff}}$, and that of the lower path increases by $n\hbar k_{\text{eff}}$. After time $T$ again, a Bragg $\pi/2$ pulse is added, and atoms from the different paths interfere with each other. After going through these processes, the probability of an atom remaining in the momentum state $|p_0\rangle$ is $(1 + C\cos(\Delta\phi))/2$, where $C$ is the contrast of the fringe, and $\Delta\phi$ is the phase difference accumulated by the two interference arms. When the atom is free-falling in a uniform gravity field, $\Delta\phi$ can be expressed as

$$\Delta\phi = n(\vec{k}_{\text{eff}} \cdot \vec{g} - \alpha)T^2, \tag{1}$$

where $\vec{g}$ is the local gravitational acceleration due to the Earth, $\alpha$ is the frequency chirp rate of the Bragg laser to compensate the Doppler effect, and $T$ is the time interval between the Bragg $\pi$ and $\pi/2$ pulses. We can see that all the terms in Eq. (1) are known except for gravity $\vec{g}$ and phase $\Delta\phi$. If we know the value of the phase, we can calculate the gravity from Eq. (1).

We can obtain the phase $\Delta\phi$ by fitting the interference fringes, where the fringe contrast of an interferometer is an important factor limiting the resolution of the result. The more efficient the Bragg pulse, the higher the fringe contrast. It is therefore necessary to suppress the thermal expansion of the atomic cloud in the transverse direction, and prevent the Bragg pulse efficiency decreasing due to atom diffusion. To achieve a high-contrast interference fringe, we use the RSC to cool the atoms in the transverse direction.

### B. Testing Lorentz violation

As mentioned above, the violation of LLI in the gravity sector suggests that the gravity between two bodies depends on the orientation and motion of their separation. Within the post-Newtonian treatment, the Lagrangian for the gravitational interaction of a two-body system in the minimal standard model extension of the pure-gravity sector can be written as [41]

$$L^T = \frac{1}{2}mv^2 + G\frac{Mm}{2r}(2 + 3\bar{s}^{00} + \bar{s}^{jk}\hat{r}^j\hat{r}^k - 3\hat{s}^{0j}v^j - \bar{s}^{0j}\hat{r}^j v^k\hat{r}^k), \tag{2}$$
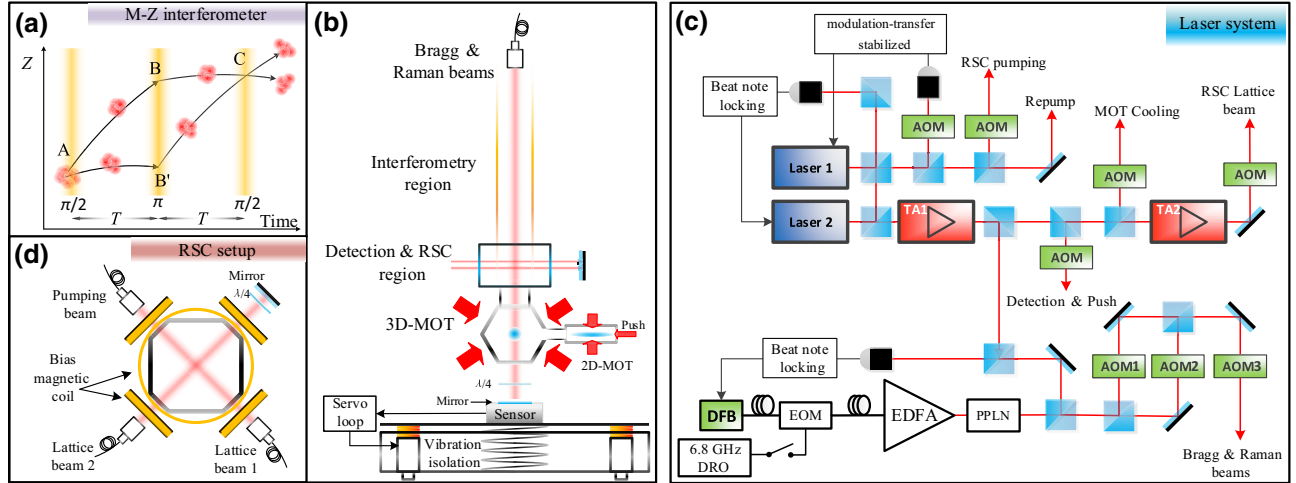


FIG. 1. (a) The space-time diagram of the Mach-Zehnder type atom interferometer. (b) Schematic experimental setup of our atom interferometer. (c) Schematic setup of our laser system. The laser 1 is locked to the $|F = 1\rangle \rightarrow |F' = 2\rangle$ transition of $^{87}$Rb $D_2$ lines. The laser 2 is locked to the $|F = 2\rangle \rightarrow |F' = 3\rangle$ transition of $^{87}$Rb $D_2$ lines with a red detuning of 242 MHz. The 1560-nm laser was amplified after injection of an Er-doped fiber amplifier (EDFA). Then the output laser from the EDFA is frequency-doubled through a periodically poled magnesium-oxide-doped lithium niobate (PPLN) crystal. We then split it in two to act as Bragg beams. The Raman beams are generated by an electro-optic modulator (EOM) driven by a dielectric resonator oscillator (DRO) operating at 6.8 GHz. (d) Top view of the experimental setup for the RSC at the detection region.

where $j, k$ denote the space coordinates, $\vec{v}$ is the relative velocity, $\hat{r} = \vec{r}/r$, and $s^{\mu\nu}$ are the fields contributing to Lorentz violation. The reference frame chosen here is the laboratory frame $(t, x^j = x, y, z)$.

After appropriate transformation into the Sun-centered frame, we can obtain the time dependence of the $g$ modulations [41]:

$$\frac{\delta g}{g_0} = \sum C_m \cos(\omega_m t + \phi_m) + D_m \sin(\omega_m t + \phi_m). \quad (3)$$

The coefficients $C$ and $D$ are functions of $s^{\mu\nu}$, corresponding to the six frequencies $\omega$, $2\omega$, $\omega \pm \Omega$, and $2\omega \pm \Omega$, where $\omega$ and $\Omega$ are the angular frequency of the Earth's rotation and of the Earth's orbit, $\omega = 2\pi/23.93$ h and $\Omega = 2\pi/1$ yr. The phase $\phi = \omega(t_l - t_c)$ is the difference between celestial time $t_c$ and laboratory time $t_l$ [42]. The functional relations of coefficients $C_m$ and $D_m$ with $s^{\mu\nu}$ are given in Refs. [31,32,41]; we can solve the coefficients $s^{\mu\nu}$ from these components.

## III. EXPERIMENTS

### A. Transverse cooling with the RSC

The configuration of the experimental setup is schematically shown in Fig. 1(b). We use a two-dimensional magneto-optical trap (2D-MOT) to load atoms, and a three-dimensional magneto-optical trap (3D-MOT) to trap and cool atoms, with a total number of $10^9$ atoms in 200 ms loading time. Then atoms are launched by increasing the frequency of upward lasers. Below the 3D-MOT is an active vibration isolation system to reduce the impact of ground vibration on the experiment [4,43].

The laser system used in the experiment is modified from the optics used in our previous work [39], as shown in Fig. 1(c). The laser 1 is locked on the $|5\,^2S_{1/2}, F = 1\rangle \rightarrow |5\,^2P_{3/2}, F' = 2\rangle$ transition of $^{87}$Rb by modulation-transfer stabilization, and it is used as the repump beam. Then, using an acoustic optical modulator (AOM), we shift its frequency to the $|5\,^2S_{1/2}, F = 1\rangle \rightarrow |5\,^2P_{3/2}, F' = 0\rangle$ transition for the RSC pumping beam. The laser 2 is locked to the $|5\,^2S_{1/2}, F = 2\rangle \rightarrow |5\,^2P_{3/2}, F' = 3\rangle$ transition lines with a red detuning of 242 MHz using the laser 1 as a reference. Then it is amplified by a Toptica BoosTA (TA), and we shift its frequency to work as the detection beam, push beam, and MOT cooling beam. The laser 2 is also used as the reference laser to lock the frequency of the distributed feedback (DFB) laser at 1560 nm. The DFB laser is stabilized with a red detuning of 3.1 GHz to the $|5\,^2S_{1/2}, F = 2\rangle \rightarrow |5\,^2P_{3/2}, F' = 3\rangle$ transition after frequency doubling.

In addition, we isolate a portion of the laser from TA1 and amplify it with TA2, and then shift its frequency to form a lattice laser for the RSC. The lattice laser and RSC pumping laser come in through a diagonal window in the detection region, as shown in Fig. 1(d). The lattice is composed of a standing wave and a traveling wave. Using $p$ light beams, one can form an optical lattice of $n$ dimensions ($p > n$) [44,45]. The frequency of the lattice laser for the RSC used in the experiment is red-detuned by 121 MHz from the $|F = 2\rangle \rightarrow |F' = 3\rangle$ transition in the $^{87}$Rb $D_2$ line. This laser not only acts as a lattice light to trap the atom which is in the $|F = 1\rangle$ state, but also pumps the atom from $|F = 2\rangle$ to $|F = 1\rangle$.

When the atoms reach the detection region, we pump the atoms from $|5\,^2S_{1/2}, F = 2\rangle$ to $|5\,^2S_{1/2}, F = 1\rangle$ using the lattice laser, as shown in Fig. 2(a). Then we use the RSC to reduce the temperature of the atoms in the transverse direction while they are moving into the detection region. The RSC can be done in a few milliseconds, although the temperature obtained after the RSC is not as low as that of evaporative cooling [46–48], but the RSC does not take so much cooling time and can keep a large number of atoms. We only need to turn on the lattice light, pump light, and magnetic field at the appropriate times to cool the atoms.

The RSC of cold atoms has been described in Ref. [49]. The principle of the RSC can be shown as in Fig. 2(b). Atoms in the lower hyperfine state $|F = 1\rangle$ are adiabatically loaded into a lattice site and occupy a set of vibrational states according to its initial momentum. If the Zeeman splitting $g_F \mu_B B$ between the magnetic sublevels of $^{87}$Rb is equal to the vibrational splitting $\hbar\omega_{\text{vib}}$, the different vibrational state and magnetic sublevels are then pairwise degenerate, i.e., $|\nu = 0, F = 1, m_F = -1\rangle$ and $|\nu = 1, F = 1, m_F = 0\rangle$ have the same energy. Once these levels are degenerate, two-photon degenerate Raman transitions allow coupling between these levels. The lattice laser can provide photons for the transition if the frequency
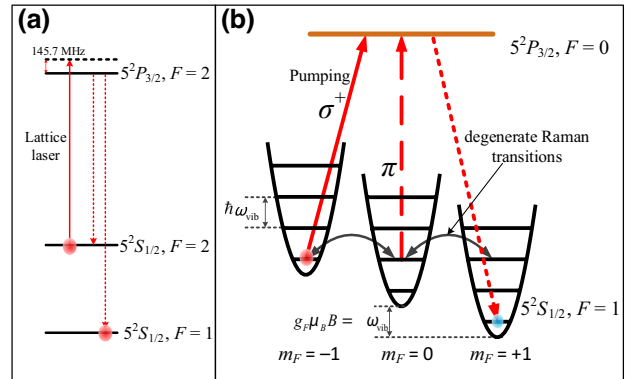


FIG. 2. (a) The atomic transition line from $|F = 2\rangle$ to $|F' = 2\rangle$ and then spontaneous emission to the dark state $|F = 1\rangle$. (b) Schematic of Raman sideband cooling, $\sigma^+$, and $\pi$ is the pumping laser. The Zeeman splitting is equal to the vibrational splitting of the lattice to form the degenerate Raman transition. Because the energy of vibrational level splitting is much greater than that of photon recoil, spontaneous emission will not change the vibrational state of the atom in the lattice.

is appropriate. The atoms then transition to the excited state $|F' = 0\rangle$ through the light which has $\sigma^+$ polarization. If it undergoes spontaneous emission to the $|v = 0,\ F = 1,\ m_F = 1\rangle$ state, the atoms are cooled because the energy absorbed is less than that emitted.

## B. Evaluating the effect of the RSC

The RSC is performed in the transverse direction and the signal obtained by our detection system reflects the longitudinal distribution of atoms. Thus we can indirectly infer the effect of transverse cooling by measuring the number of atoms returning to the detection region. After the atoms are launched, we use microwave pulses to select the atoms to $|5\ ^2S_{1/2},\ F = 1,\ m_F = 0\rangle$, and then blow away the remaining atoms in $|5\ ^2S_{1/2},\ F = 2\rangle$. After this, the TOF signal with and without the RSC is shown in Fig. 3(a).

It can be seen from Fig. 3(a) that the TOF signal becomes 2.75 times larger after adding the RSC. When an atomic cloud with horizontal temperature $T_e$ passes through a probe laser of width $l$ in the detection region, we can calculate the amplitude of the TOF signal from the formula

$$\frac{A}{w_{T_e}} \int_{-l/2}^{l/2} \exp\left[ -2\left( \frac{x}{w_{T_e}} \right)^2 \right] dx,$$

where $A$ is the scaling factor, $x$ is the horizontal position coordinate of the atom (where the origin of the coordinate system is in the center of the probe laser), and $w_{T_e}$ is the width of the atomic cloud in the horizontal direction. In our experiment, without the RSC, the atom temperature is 12.5 μK. Ignoring the initial size of the atomic cloud, we calculated the relative amplitude $A/A_{12.5\ \mu K}$ of the TOF signals of atoms at different horizontal temperatures using the TOF signal amplitude $A_{12.5\ \mu K}$ of atoms at a horizontal temperature of 12.5 μK as a reference, and the results

are shown in Fig. 3(b). It is found that, when the TOF signal is 2.75 times stronger, the atoms' temperature in the horizontal direction is 0.85 μK.

## C. Atomic state preparation

After we pump the atoms to $|5\ ^2S_{1/2},\ F = 1\rangle$ and use the RSC, most of the atoms are in the magnetically sensitive state $|5\ ^2S_{1/2},\ F = 1,\ m_F = 1\rangle$. In order to perform the interferometric experiment, we need to prepare the atoms in the magnetically insensitive state $|5\ ^2S_{1/2},\ F = 1,\ m_F = 0\rangle$. We use a linearly polarized laser with frequency resonant with the $|5\ ^2S_{1/2},\ F = 1\rangle \rightarrow |5\ ^2P_{3/2}, F' = 0\rangle$ transition.

As shown in Fig. 4(a), the direction of laser propagation is nearly parallel to the magnetic field, so the $\pi$ transition has a considerably lower probability than the $\sigma^\pm$ transition, and the atom in the $|5\ ^2S_{1/2},\ F = 1,\ m_F = \pm1\rangle$ state will be driven to the excited state $|5\ ^2P_{3/2},\ F' = 0\rangle$ and then spontaneously radiate to the dark state $|5\ ^2S_{1/2},\ F = 1,\ m_F = 0\rangle$. We then use a microwave pulse to select it to $|5\ ^2S_{1/2},\ F = 2,\ m_F = 0\rangle$, and blow away the remaining atoms in $|5\ ^2S_{1/2},\ F = 1\rangle$. After these steps, we apply a Doppler-sensitive Raman pulse with a duration of 300 μs to transform the atoms to the state $|5\ ^2S_{1/2},\ F = 1,\ m_F = 0\rangle$ with a narrow velocity distribution.

After the state preparation and velocity selection by Raman beams, the TOF signal is as shown in Fig. 4(b). The black line is the TOF signal obtained by the microwave pulse selection and velocity selection with the Raman pulse. In fact, if no RSC is performed, by pumping the atoms of the $|F = 2\rangle$ state to the $|F = 1\rangle$ state and then using optical pumping to pump them all to the magnetically insensitive state, such a state selection yields five times more atoms compared to the microwave pulse state selection. (The $|F = 2\rangle$ state has five magnetic energy levels, and the microwave pulse can select only 1/5 of the atoms.) The TOF signal thus obtained is shown as the blue dashed line in Fig. 4(b). If the RSC is added to this, it is theoretically able to increase the number of atoms returning to the detection region by a factor of $5 \times 2.75$. However, the optical pumping could also heat the atoms, which may
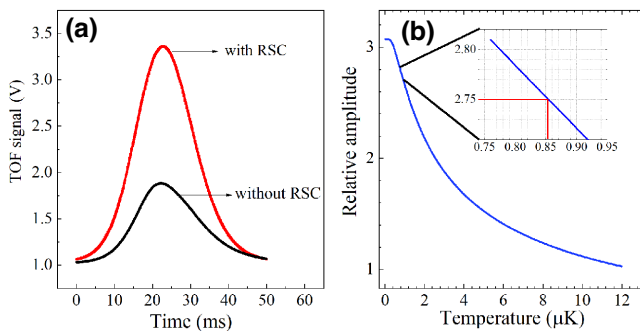
FIG. 3. (a) The amplitude of the TOF signal with or without the RSC. (b) The relative amplitude of TOF signals of atoms at different temperatures along the horizontal plane, using the TOF signal of atoms at a temperature of 12.5 μK as a reference. The enlarged inset is close to our experimental results.
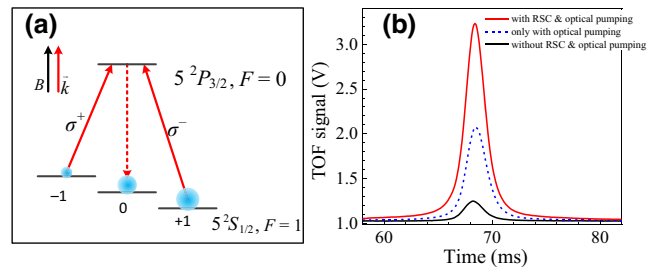
FIG. 4. (a) Preparing the atoms in the magnetically insensitive state by optical pumping. (b) The TOF signal after the initial state preparation.

reduce the effectiveness of the RSC, so the number of atoms returning to the detection region increases by only a factor of 10, as shown by the red line in Fig. 4(b).

### D. Atom interference and detection

When the atoms are prepared to the $|F = 1, \ m_F = 0\rangle$ state and enter the interferometry region, we construct a Mach-Zehnder interferometer by applying a $\pi/2$-$\pi$-$\pi/2$ Bragg pulse sequence as described in Sec. II A. In our experiment, we chose the first-order Bragg diffraction $n = 1$. After the atoms fall back into the detection region, we use the Raman spectroscopy detection method to detect atoms in different momentum states [39]. This method uses Raman pulses to select atoms with different momentum states and detect them separately, which can avoid the problem that atoms with different momenta overlap in space due to insufficient separation time.

### IV. EXPERIMENTAL RESULTS

#### A. Results of gravity measurements

We modulate the free evolution time $T$ to find the central fringe, as shown in Fig. 5. The frequency chirp rate $\alpha$ at the central fringe satisfies the equation $\alpha = \vec{k}_{\text{eff}} \cdot \vec{g}$. Figure 5 shows that the interference fringes have about 56% contrast at $T = 110$ ms, 45% at $T = 210$ ms, and 28% at $T = 320$ ms.

After determining the position of the central fringe, we can determine the experimental parameters for monitoring the gravitational acceleration. Our typical gravity measurement results by this Bragg atom interferometer are shown in Fig. 6. We apply the fringe lock method [50] to measure the gravity with a sample rate of 1 Hz. A continuous gravitational acceleration measurements for 30 h is shown in Fig. 6(a). The experimental data are consistent with the Earth tide model (red curve). The residual acceleration shown in Fig. 6(b) proves that our atom gravimeter works, with good stability.

The Allan deviation of the residual acceleration is illustrated in Fig. 6(c), which shows that the atom gravimeter
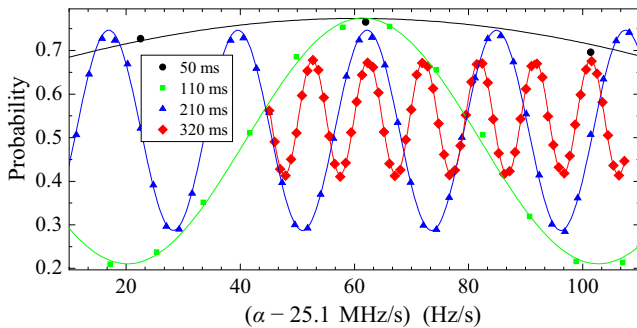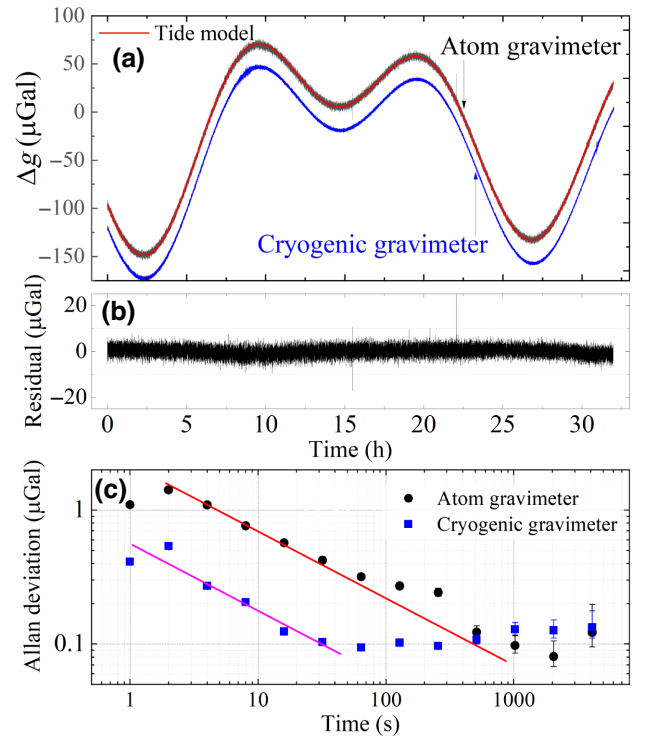


FIG. 6. (a) A continuous gravity monitor of more than 30 h on December 23 and 24, 2021. The red curve is the Earth's tide model; the black and blue lines represent the Bragg atom gravimeter results and the cryogenic gravimeter results, respectively. The offset between the last two was manually added for better visualization of the data. (b) The residual error of the experimental data. (c) Allan deviation of the $g$ measurement. Black dots: the Allan deviation of the Bragg atom gravimeter. Blue squares: the Allan deviation of the cryogenic gravimeter.

has achieved a sensitivity of 2.2 $\mu$Gal/Hz$^{1/2}$. After an integration time of 2000 s, the resolution can reach 0.08 $\mu$Gal. Comparing our gravity measurements with those of a neighboring laboratory's iGrav40 (a cryogenic superconducting relative gravimeter that boasts high sensitivity and excellent long-term stability [51]), it can be seen that, after an integration time of 500 s, the resolution of our gravimeter is comparable to that of the cryogenic gravimeter. Although the superconducting gravimeter boasts excellent sensitivity, it operates as a relative gravimeter, with its output voltage signal being directly proportional to changes in gravity. Therefore, it requires calibration using an absolute gravimeter.

#### B. Noise tracking of gravity measurement

In order to determine the main noise limits for our experiments, we evaluated the noise of each module of the system. There are three dominant noise sources in our Bragg interferometer: vibration noise, detection noise, and the phase noise of Bragg beams.



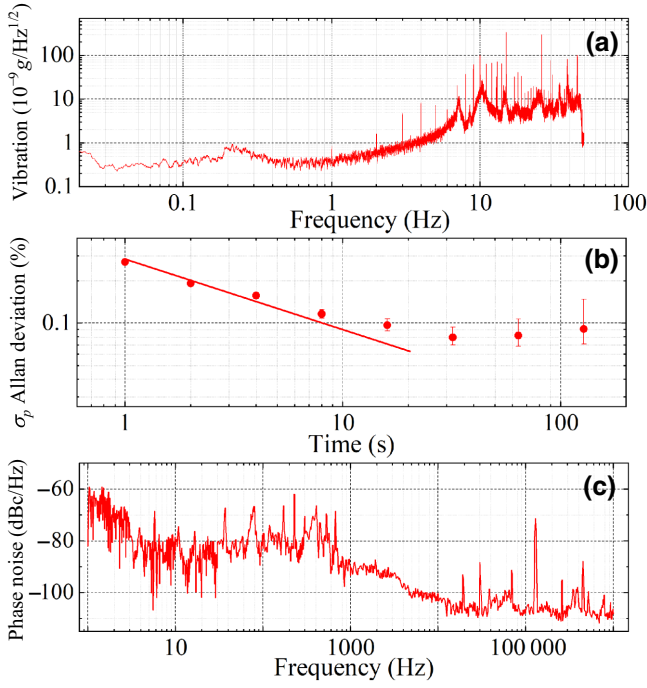FIG. 5. Interference fringes at different free evolution time $T$.

FIG. 7.   (a) The vibration noise spectrum of the reflector mirror in our experiment. (b) The population fluctuation of the atoms in one of the momentum states. (c) The phase noise of the Bragg beam in our experiment.

TABLE I.   The main noise sources in our Bragg atom gravimeter.

| Noise source | $\sigma_g$ ($\mu$Gal/Hz$^{1/2}$) |
| --- | --- |
| Vibration noise | 0.7 |
| Detection noise | 1.1 |
| Phase noise of the Bragg beams | 1.9 |
| Total | 2.3 |

vibration noise is about 0.7 $\mu$Gal/Hz$^{1/2}$ for a common condition.

The detection methods in our experiment have been described in detail in Ref. [39]. The total contribution of the detection noise to the interference phase can be expressed as $\sigma_\phi = 2\sigma_p/C$, where $C$ is the interferometer contrast and $\sigma_p$ is the fluctuation of transition probability. The contrast is about 28% for the case of $T = 320$ ms in our experiment. The detection noise $\sigma_p$ can be characterized by the population fluctuation of the atoms in one of the momentum states, as shown in Fig. 7(b), so the uncertainty of the transition probability $\sigma_p$ contributes 1.1 $\mu$Gal/Hz$^{1/2}$ to the sensitivity of the gravity measurement.

Another noise source that contributes considerably to the interference phase is the phase noise of the Bragg beam, which mainly comes from the variations in optical path length of the two Bragg beams. The spectrum of the phase noise of our Bragg beam is shown in Fig. 7(c). We can calculate its contribution to the sensitivity of gravity measurement by the method mentioned in Refs. [52,53]. The corresponding noise contribution is 1.9 $\mu$Gal/Hz$^{1/2}$. The main noise limits to the Bragg atom gravimeter are listed in Table I.

### C. Result of testing Lorentz violation

We use gravity data that span approximately 170 days to bound the Lorentz violation, shown in Fig. 8. The Fourier components $C_m$ and $D_m$ can be estimated by a least-squares

Since the phase acquired by the interaction of the atoms with the Bragg beam varies with the position of the atoms relative to the reflector, the reflector vibrations at the bottom of the instrument will directly contribute to the measurement result. We place the reflector on a vibration isolation platform and use a feedback technique to suppress platform vibrations, as shown in Fig. 1(b). The vibration noise spectrum after vibration isolation is shown in Fig. 7(a). When $T = 320$ ms, the contribution of the
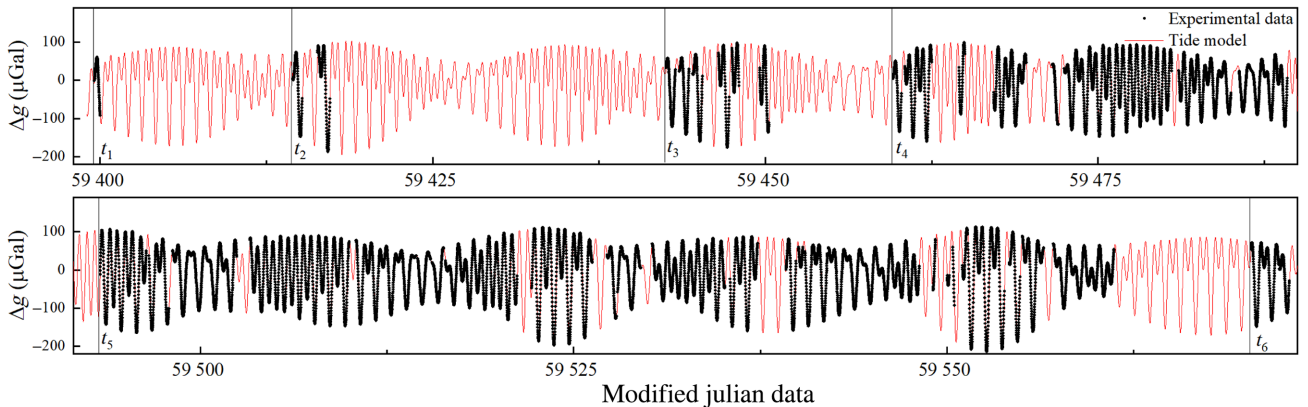


FIG. 8.   Tide data from July, 2021 to December, 2021. Each point of the gravity data recorded by the atom gravimeter is the average of 600 s data. The black dots represent experimental data, while the red line represents the tide model.
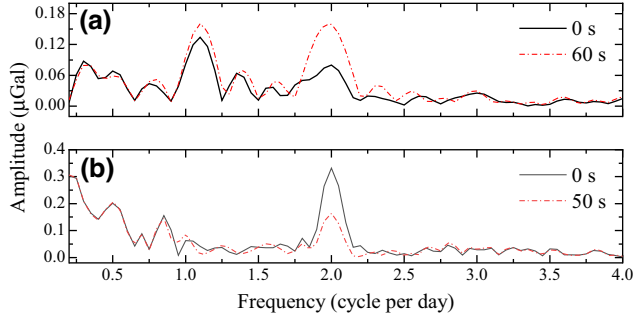
FIG. 9. (a) The amplitude spectrum of the gravity residual on September 16, 2021. The spectrum becomes larger at $2\omega$ when the initial time delay of 60 s is added. (b) The frequency spectrum on November 10, 2021. The spectrum becomes smaller at $2\omega$ when the initial time delay of 50 s is added.



FIG. 10. The variation of the space-space component coefficients $s^{\mu\nu}$ with initial time $t_4$ and $t_5$. The coefficients vary linearly with time.

fit using the residual data and Eq. (3). We can then solve for the coefficients $s^{\mu\nu}$ from these Fourier components.

For our experiment, there are two main errors in the calculation of the coefficients: one is the fitting error from the least-squares fitting, and the other is the error caused by the misalignment of the experimental time. Once the gravity data have been obtained, it is critical to determine the exact Coordinated Universal Time (UTC) at the start of the experiment for accurate tide correction. Because of the offline operation of our equipment and lack of time calibration (our laboratory is located in a cave without Internet and with no Global Positioning System signals), we were unable to determine the exact UTC at the start of the experiment. As a result, the residual gravity data obtained after subtracting tide signals is not entirely precise, potentially affecting the accuracy of the final evaluation results. We vary the initial time of the gravity data and get different spectra of residuals, as shown in Fig. 9, which indicates that the error in the starting time of the experiment has a significant effect on the results.

In our experiment, the time interval for each shot in the experiment is referenced to the rubidium clock, while the UTC at the beginning of the experiment was inferred from the computer clock. When there is a gap of several days between experiments,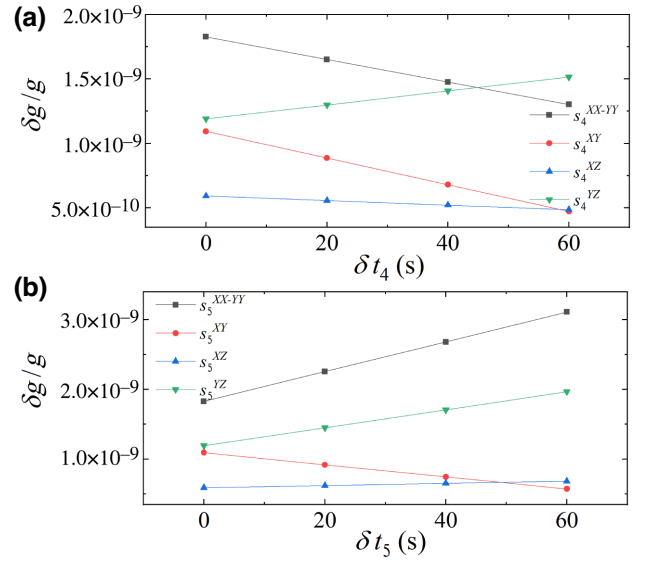 the time misalignment error in the computer will be different compared to the previous observation. The experimental data used for the LLI test consist of six sets of independent gravity observations at different times, corresponding to $t_i$ $(t_1, \ldots, t_6)$, as shown in Fig. 8. By adding the time delay $\delta t_i$ to the initial time of the laboratory measurement data, and then calculating the tidal signal, the different residuals were obtained. Then we can calculate the coefficients $s_i^{\mu\nu}$. The proportion of the time error transferred to the coefficient was calculated, so as to obtain the contribution of the time error to the calculation result. For example, Fig. 10 shows the variation of the coefficients $s_i^{\mu\nu}$ after varying the initial time $t_4$ and $t_5$. We can see from the figure that $s_i^{\mu\nu}$ varies linearly with $\delta t_i$, so the error introduced by the time misalignment is $\delta s_i^{\mu\nu} = \delta t_i \, \partial s_i^{\mu\nu}/\partial t_i$, and the total error caused by the time misalignment is $\sqrt{\sum_i (\delta t_i \, \partial s_i^{\mu\nu}/\partial t_i)^2}$. In our experiments, since the computer time has not been calibrated by the Internet, the start time of the experiment has about one-minute uncertainty relative to UTC.

TABLE II. The components of Lorentz violation ($\delta_g/g$) from our experimental result ($2\sigma$).

| Coefficient | This work | By atom gravimeter in 2009 [31] | By pulsar analysis in 2014 [36] |
|---|---|---|---|
| $\bar{s}^{TX}$ | $(3.4 \pm 7.9) \times 10^{-6}$ | $(-3.1 \pm 5.1) \times 10^{-5}$ | $(-5.2 \pm 5.3) \times 10^{-9}$ |
| $\bar{s}^{TY}$ | $(7.8 \pm 12.1) \times 10^{-6}$ | $(0.1 \pm 5.4) \times 10^{-5}$ | $(-7.5 \pm 8.5) \times 10^{-9}$ |
| $\bar{s}^{TZ}$ | $(-7.2 \pm 9.8) \times 10^{-6}$ | $(1.4 \pm 6.6) \times 10^{-5}$ | $(-5.9 \pm 5.8) \times 10^{-9}$ |
| $\bar{s}^{XX} - \bar{s}^{YY}$ | $(1.8 \pm 2.1) \times 10^{-9}$ | $(4.4 \pm 11) \times 10^{-9}$ | $(-9.7 \pm 10.1) \times 10^{-11}$ |
| $\bar{s}^{XY}$ | $(1.1 \pm 1.0) \times 10^{-9}$ | $(0.2 \pm 3.9) \times 10^{-9}$ | $(-3.5 \pm 3.6) \times 10^{-11}$ |
| $\bar{s}^{XZ}$ | $(5.9 \pm 5.5) \times 10^{-10}$ | $(-2.6 \pm 4.4) \times 10^{-9}$ | $(-2.0 \pm 2.0) \times 10^{-11}$ |
| $\bar{s}^{YZ}$ | $(1.2 \pm 1.1) \times 10^{-9}$ | $(-0.3 \pm 4.5) \times 10^{-9}$ | $(-3.3 \pm 3.3) \times 10^{-11}$ |

The limits and corresponding errors for Lorentz violation given by the calculation are listed in Table II. The errors presented here include the time misalignment error and the least-squares fitting error. The errors in the table are a combination of these two errors. The space-space components are improved by about four times compared to previous measurements with atom interferometers [31]. We compared our results with those obtained from pulsar analysis [36], which is currently the most effective method for testing LLI in the gravity sector. The results obtained from pulsar analysis are several orders of magnitude more precise than those from the gravity data analysis, as the LLI violations in the latter arise from the rotation and revolution of the Earth, while the pulsars are not subject to this limitation.

## V. CONCLUSION AND OUTLOOK

In conclusion, we have demonstrated a precision Bragg atom gravimeter with a sensitivity of $2.2\,\mu\mathrm{Gal/Hz}^{1/2}$. With an integration time of 2000 s, a resolution of $0.08\,\mu\mathrm{Gal}$ can be achieved, which is comparable to the resolution of a cryogenic superconducting gravimeter. This work improves upon our previously constructed interferometer [4] and sets a new record on the sensitivity for an atom-interferometry absolute gravimeter.

We also evaluate the limit of Lorentz violation with gravity data measured by this atom gravimeter. The precision of the LLI test by the gravity data is further improved. The test precision is limited by the mismatch between the experimental time and UTC. However, this effect is not intrinsic to the method but can be mitigated by periodically calibrating the time manually.

So far, the phase noise of the Bragg beam is the most significant limitation to the sensitivity. In the future, the phase noise of the Bragg beam can be suppressed by using an optical phase-locked loop. The scale factor can be increased by increasing the momentum difference between the interference paths. The state preparation method mentioned in this work effectively improves the signal-to-noise ratio of the interferometer and can be applied to different types of atom interferometers. The Bragg atom gravimeter shows great potential for high-precision experiments.

[1] A. Peters, K. Y. Chung, and S. Chu, Measurement of gravitational acceleration by dropping atoms, Nature **400,** 849 (1999).

[2] A. Louchet-Chauvet, T. Farah, Q. Bodart, A. Clairon, A. Landragin, S. Merlet, and F. P. Dos Santos, The influence of transverse motion within an atomic gravimeter, New J. Phys. **13,** 065025 (2011).

[3] P. Gillot, O. Francis, A. Landragin, F. P. Dos Santos, and S. Merlet, Stability comparison of two absolute gravimeters: Optical versus atomic interferometers, Metrologia **51,** L15 (2014).

[4] Z.-K. Hu, B.-L. Sun, X.-C. Duan, M.-K. Zhou, L.-L. Chen, S. Zhan, Q.-Z. Zhang, and J. Luo, Demonstration of an ultrahigh-sensitivity atom-interferometry absolute gravimeter, Phys. Rev. A **88,** 043610 (2013).

[5] C. Freier, M. Hauth, V. Schkolnik, B. Leykauf, M. Schilling, H. Wziontek, H.-G. Scherneck, J. Müller, and A. Peters, in *Journal of Physics: Conference Series*, Vol. 723 (IOP Publishing, 2016), p. 012050.

[6] M. Snadden, J. McGuirk, P. Bouyer, K. Haritos, and M. Kasevich, Measurement of the Earth's Gravity Gradient with an Atom Interferometer-Based Gravity Gradiometer, Phys. Rev. Lett. **81,** 971 (1998).

[7] I. Dutta, D. Savoie, B. Fang, B. Venon, C. G. Alzar, R. Geiger, and A. Landragin, Continuous Cold-Atom Inertial Sensor with 1 nrad/sec Rotation Stability, Phys. Rev. Lett. **116,** 183003 (2016).

[8] R. H. Parker, C. Yu, W. Zhong, B. Estey, and H. Müller, Measurement of the fine-structure constant as a test of the standard model, Science **360,** 191 (2018).

[9] G. Rosi, F. Sorrentino, L. Cacciapuoti, M. Prevedelli, and G. Tino, Precision measurement of the Newtonian gravitational constant using cold atoms, Nature **510,** 518 (2014).

[10] M.-K. Zhou, Z.-K. Hu, X.-C. Duan, B.-L. Sun, J.-B. Zhao, and J. Luo, Precisely mapping the magnetic field gradient in vacuum with an atom interferometer, Phys. Rev. A **82,** 061602 (2010).

[11] J. M. Hogan and M. A. Kasevich, Atom-interferometric gravitational-wave detection using heterodyne laser links, Phys. Rev. A **94,** 033632 (2016).

[12] M. A. Norcia, J. R. Cline, and J. K. Thompson, Role of atoms in atomic gravitational-wave detectors, Phys. Rev. A **96,** 042118 (2017).

[13] C. M. Will, The confrontation between general relativity and experiment, Living Rev. Relativ. **17,** 1 (2014).

[14] K. Nordtvedt, Jr., Equivalence principle for massive bodies. II. Theory, Phys. Rev. **169,** 1017 (1968).

[15] G. Amelino-Camelia, C. Lämmerzahl, A. Macias, and H. Müller, in *AIP Conference Proceedings*, Vol. 758 (American Institute of Physics, 2005), p. 30.

[16] R. F. Vessot, M. Levine, E. Mattison, E. Blomberg, T. Hoffman, G. Nystrom, B. Farrel, R. Decher, P. Eby, and C. Baugher, *et al.*, Test of Relativistic Gravitation with a Space-Borne Hydrogen Maser, Phys. Rev. Lett. **45,** 2081 (1980).

[17] H. Müller, A. Peters, and S. Chu, A precision measurement of the gravitational redshift by the interference of matter waves, Nature **463,** 926 (2010).

[18] S. Fray, C. A. Diez, T. W. Hänsch, and M. Weitz, Atomic Interferometer with Amplitude Gratings of Light and Its

Applications to Atom Based Tests of the Equivalence Principle, Phys. Rev. Lett. **93,** 240404 (2004).

[19] A. Bonnin, N. Zahzam, Y. Bidel, and A. Bresson, Simultaneous dual-species matter-wave accelerometer, Phys. Rev. A **88,** 043615 (2013).

[20] D. Schlippert, J. Hartwig, H. Albers, L. L. Richardson, C. Schubert, A. Roura, W. P. Schleich, W. Ertmer, and E. M. Rasel, Quantum Test of the Universality of Free Fall, Phys. Rev. Lett. **112,** 203002 (2014).

[21] M. G. Tarallo, T. Mazzoni, N. Poli, D. Sutyrin, X. Zhang, and G. Tino, Test of Einstein Equivalence Principle for 0-Spin and Half-Integer-Spin Atoms: Search for Spin-Gravity Coupling Effects, Phys. Rev. Lett. **113,** 023005 (2014).

[22] L. Zhou, S. Long, B. Tang, X. Chen, F. Gao, W. Peng, W. Duan, J. Zhong, Z. Xiong, and J. Wang, *et al.,* Test of Equivalence Principle at $10^{-8}$ Level by a Dual-Species Double-Diffraction Raman Atom Interferometer, Phys. Rev. Lett. **115,** 013004 (2015).

[23] L. Zhou, C. He, S.-T. Yan, X. Chen, W.-T. Duan, R.-D. Xu, C. Zhou, Y.-H. Ji, S. Barthwal, and Q. Wang, *et al.,* United test of the equivalence principle at $10^{-10}$ level using mass and internal energy specified atoms, (2019), arXiv preprint ArXiv:1904.07096.

[24] J. Hartwig, S. Abend, C. Schubert, D. Schlippert, H. Ahlers, K. Posso-Trujillo, N. Gaaloul, W. Ertmer, and E. M. Rasel, Testing the universality of free fall with rubidium and ytterbium in a very large baseline atom interferometer, New J. Phys. **17,** 035011 (2015).

[25] X.-C. Duan, X.-B. Deng, M.-K. Zhou, K. Zhang, W.-J. Xu, F. Xiong, Y.-Y. Xu, C.-G. Shao, J. Luo, and Z.-K. Hu, Test of the Universality of Free Fall with Atoms in Different Spin Orientations, Phys. Rev. Lett. **117,** 023001 (2016).

[26] K. Zhang, M.-K. Zhou, Y. Cheng, L.-L. Chen, Q. Luo, W.-J. Xu, L.-S. Cao, X.-C. Duan, and Z.-K. Hu, Testing the universality of free fall by comparing the atoms in different hyperfine states with Bragg diffraction, Chin. Phys. Lett. **37,** 043701 (2020).

[27] P. Asenbaum, C. Overstreet, M. Kim, J. Curti, and M. A. Kasevich, Atom-Interferometric Test of the Equivalence Principle at the $10^{-12}$ Level, Phys. Rev. Lett. **125,** 191101 (2020).

[28] V. A. Kosteleckỳ, Gravity, Lorentz violation, and the standard model, Phys. Rev. D **69,** 105009 (2004).

[29] V. A. Kosteleckỳ and N. Russell, Data tables for Lorentz and *CPT* violation, Rev. Mod. Phys. **83,** 11 (2011).

[30] H. Müller, S.-W. Chiow, S. Herrmann, S. Chu, and K.-Y. Chung, Atom-Interferometry Tests of the Isotropy of Post-Newtonian Gravity, Phys. Rev. Lett. **100,** 031101 (2008).

[31] K.-Y. Chung, S.-W. Chiow, S. Herrmann, S. Chu, and H. Müller, Atom interferometry tests of local Lorentz invariance in gravity and electrodynamics, Phys. Rev. D **80,** 016002 (2009).

[32] C.-G. Shao, Y.-F. Chen, R. Sun, L.-S. Cao, M.-K. Zhou, Z.-K. Hu, C. Yu, and H. Müller, Limits on Lorentz violation in gravity from worldwide superconducting gravimeters, Phys. Rev. D **97,** 024019 (2018).

[33] K. Nordtvedt, Jr., Testing relativity with laser ranging to the Moon, Phys. Rev. **170,** 1186 (1968).

[34] J. B. Battat, J. F. Chandler, and C. W. Stubbs, Testing for Lorentz Violation: Constraints on Standard-Model-Extension Parameters via Lunar Laser Ranging, Phys. Rev. Lett. **99,** 241103 (2007).

[35] A. Bourgoin, A. Hees, S. Bouquillon, C. Le Poncin-Lafitte, G. Francou, and M.-C. Angonin, Testing Lorentz Symmetry with Lunar Laser Ranging, Phys. Rev. Lett. **117,** 241301 (2016).

[36] L. Shao, Tests of Local Lorentz Invariance Violation of Gravity in the Standard Model Extension with Pulsars, Phys. Rev. Lett. **112,** 111103 (2014).

[37] V. A. Kosteleckỳ and J. D. Tasson, Constraints on Lorentz violation from gravitational Čerenkov radiation, Phys. Lett. B **749,** 551 (2015).

[38] C. Janvier, V. Ménoret, B. Desruelle, S. Merlet, A. Landragin, and F. P. dos Santos, Compact differential gravimeter at the quantum projection-noise limit, Phys. Rev. A **105,** 022801 (2022).

[39] Y. Cheng, K. Zhang, L.-L. Chen, T. Zhang, W.-J. Xu, X.-C. Duan, M.-K. Zhou, and Z.-K. Hu, Momentum-resolved detection for high-precision Bragg atom interferometry, Phys. Rev. A **98,** 043611 (2018).

[40] M. Kasevich and S. Chu, Measurement of the gravitational acceleration of an atom with a light-pulse atom interferometer, Appl. Phys. B **54,** 321 (1992).

[41] Q. G. Bailey and V. A. Kosteleckỳ, Signals for Lorentz violation in post-Newtonian gravity, Phys. Rev. D **74,** 045001 (2006).

[42] V. A. Kosteleckỳ and M. Mewes, Signals for Lorentz violation in electrodynamics, Phys. Rev. D **66,** 056005 (2002).

[43] M.-K. Zhou, Z.-K. Hu, X.-C. Duan, B.-L. Sun, L.-L. Chen, Q.-Z. Zhang, and J. Luo, Performance of a cold-atom gravimeter with an active vibration isolator, Phys. Rev. A **86,** 043630 (2012).

[44] G. Grynberg, B. Lounis, P. Verkerk, J.-Y. Courtois, and C. Salomon, Quantized Motion of Cold Cesium Atoms in Two- and Three-Dimensional Optical Potentials, Phys. Rev. Lett. **70,** 2249 (1993).

[45] I. H. Deutsch and P. S. Jessen, Quantum-state control in optical lattices, Phys. Rev. A **57,** 197 (1998).

[46] C. Kuhn, G. McDonald, K. Hardman, S. Bennetts, P. Everitt, P. Altin, J. Debs, J. Close, and N. Robins, A Bose-condensed, simultaneous dual-species Mach–Zehnder atom interferometer, New J. Phys. **16,** 073035 (2014).

[47] K. Kotru, D. L. Butts, J. M. Kinast, and R. E. Stoner, Large-Area Atom Interferometry with Frequency-Swept Raman Adiabatic Passage, Phys. Rev. Lett. **115,** 103001 (2015).

[48] H. Zhang, X. Ren, W. Yan, Y. Cheng, H. Zhou, Z. Gao, Q. Luo, M. Zhou, and Z. Hu, Effects related to the temperature of atoms in an atom interferometry gravimeter based on ultra-cold atoms, Opt. Express **29,** 30007 (2021).

[49] A. J. Kerman, V. Vuletić, C. Chin, and S. Chu, Beyond Optical Molasses: 3D Raman Sideband Cooling of Atomic Cesium to High Phase-Space Density, Phys. Rev. Lett. **84,** 439 (2000).

[50] P. Cheinet, F. Pereira Dos Santos, T. Petelski, J. Le Gouët, J. Kim, K. Therkildsen, A. Clairon, and A. Landragin, Compact laser system for atom interferometry, Appl. Phys. B **84,** 643 (2006).

[51] R. Warburton, H. Pillai, and R. Reineman, in *Extended Abstract Presented at 2nd Asia Workshop on Superconducting Gravimetry Taipei, Taiwan* (2010).

[52] J. Le Gouët, T. Mehlstäubler, J. Kim, S. Merlet, A. Clairon, A. Landragin, and F. Pereira Dos Santos, Limits to the sensitivity of a low noise compact atomic gravimeter, Appl. Phys. B **92,** 133 (2008).

[53] T. Mazzoni, X. Zhang, R. Del Aguila, L. Salvi, N. Poli, and G. Tino, Large-momentum-transfer Bragg interferometer with strontium atoms, Phys. Rev. A **92,** 053619 (2015).